Prediction of Intracranial Aneurysm Rupture Risk Using Non-Invasive Radiomics Analysis Based on Follow-Up Magnetic Resonance Angiography Images: A Preliminary Study

山之内, 雅幸

https://hdl.handle.net/2324/6787457

出版情報：Kyushu University, 2022, 博士（保健学）, 課程博士
バージョン：

applied sciences

MDPI

Article

Prediction of Intracranial Aneurysm Rupture Risk Using Non-Invasive Radiomics Analysis Based on Follow-Up Magnetic Resonance Angiography Images: A Preliminary Study

Masayuki Yamanouchi [1,2], Hidetaka Arimura [3,*], Takumi Kodama [1] and Akimasa Urakami [1]

[1] Division of Medical Quantum Science, Department of Health Sciences, Graduate School of Medical Sciences, Kyushu University, Fukuoka 819-0395, Japan
[2] Kokura Memorial Hospital, 3-2-1 Asano, Kokurakita-ku, Kitakyushu-shi 802-8555, Japan
[3] Division of Medical Quantum Science, Department of Health Sciences, Faculty of Medical Sciences, Kyushu University, 3-1-1 Maidashi, Higashi-ku, Fukuoka 812-8582, Japan
* Correspondence: arimura.hidetaka.616@m.kyushu-u.ac.jp

Featured Application: To prevent subarachnoid hemorrhage (SAH), aneurysms should be appropriately treated at the right time by predictively monitoring the rupture risks of intracranial aneurysms using the proposed radiomics approach with non-invasive follow-up magnetic resonance angiography (MRA).

Abstract: This is the first preliminary study to develop prediction models for aneurysm rupture risk using radiomics analysis based on follow-up magnetic resonance angiography (MRA) images. We selected 103 follow-up images from 18 unruptured aneurysm (UA) cases and 10 follow-up images from 10 ruptured aneurysm (RA) cases to build the prediction models. A total of 486 image features were calculated, including 54 original features and 432 wavelet-based features, within each aneurysm region in the MRA images for the texture patterns. We randomly divided the 103 UA data into 50 training and 53 testing data and separated the 10 RA data into 1 test and 9 training data to be increased to 54 using a synthetic minority oversampling technique. We selected 11 image features associated with UAs and RAs from 486 image features using the least absolute shrinkage and the selection operator logistic regression and input them into a support vector machine to build the rupture prediction models. An imbalanced adjustment training and test strategy was developed. The area under the receiver operating characteristic curve, accuracy, sensitivity, and specificity were 0.971, 0.948, 0.700, and 0.953, respectively. This prediction model with non-invasive MRA images could predict aneurysm rupture risk for SAH prevention.

Keywords: intracranial aneurysms; rupture risk; prediction model; radiomics; magnetic resonance angiography

check for updates

Citation: Yamanouchi, M.; Arimura, H.; Kodama, T.; Urakami, A. Prediction of Intracranial Aneurysm Rupture Risk Using Non-Invasive Radiomics Analysis Based on Follow-Up Magnetic Resonance Angiography Images: A Preliminary Study. *Appl. Sci.* **2022**, *12*, 8615. https://doi.org/10.3390/app12178615

Academic Editors: Atsushi Teramoto and Tomoko Tateyama

Received: 23 July 2022
Accepted: 24 August 2022
Published: 28 August 2022

1. Introduction

The rupture of intracranial aneurysms causes a subarachnoid hemorrhage (SAH), which occurs in 85% of patients with aneurysms [1]. According to a large Japanese cohort study (6697 aneurysms) [2], the average age of aneurysm patients is 63 in Japan, and the risk factors for aneurysm ruptures were age (≥70), female sex, hypertension, size (≥7 mm), and location. Approximately 50% of patients die of first bleeding after an SAH, and the other half die of rebleeding or a cerebral vasospasm [3]. Preventive treatments for unruptured aneurysms (UAs) such as surgery (surgical clipping) and endovascular treatment (coil embolization) should be performed at the right time; however, there are risks of postoperative sequelae in approximately 1.9–12% of patients [3]. Therefore, it should be carefully decided whether to treat or to monitor UAs [4] by predicting rupture risks. Furthermore, the monitoring approaches should be non-invasive because of their sustainability.

If the aneurysm rupture risk can be non-invasively predicted, then preventive treatments can be carried out for high-risk patients, but unnecessary treatments can be avoided for low-risk patients.

Magnetic resonance angiography (MRA) can non-invasively detect and monitor unruptured intracranial aneurysms (mean detection rate: 96%) for follow-up purposes without the use of a contrast agent or exposure of patients to radiation [5]. On the contrary, computed tomography angiography (CTA) requires a contrast agent and X-rays, but it can be utilized for detecting and monitoring unruptured intracranial aneurysms. MRA using a high magnetic field 3.0 Tesla MRI device has 99.3% sensitivity and 96.9% specificity for aneurysm detection [6], and there is no significant difference in the sensitivity and specificity between MRA and CTA [7]. Therefore, the prediction or monitoring of an aneurysm rupture risk based on non-invasive MRA is more appropriate. Moreover, computational prediction approaches should be developed in quantitative ways to mitigate intra- and inter-observer variability [8].

In recent years, radiomics studies have been performed to predict aneurysm rupture risk using CTA and digital subtraction angiography (DSA) [9–17]. Liu et al. evaluated the feasibility of applying machine learning to predict aneurysm stability with morphological features derived from radiomics based on DSA [9]. Ludwig et al. assessed the performance of radiomics-derived morphological features in predicting aneurysm rupture status using DSA [10]. Alwalid et al. developed a CTA-based radiomics approach for the classification of intracranial aneurysm ruptures [11]. Zhu et al. aimed to determine robust radiomic features associated with middle cerebral artery (MCA) aneurysm ruptures and evaluate the additional value of combining morphological and radiomic features in the classification of ruptured MCA aneurysms [12]. Tong et al. developed and validated a morphology-based radiomic signature nomogram to assess the risk of aneurysm ruptures [13]. Ou et al. evaluated the radiomic differences between ruptured and unruptured aneurysms and explored their potential use in predicting aneurysm ruptures with CTA [14] and developed deep learning models with a limited amount of labeled data for predicting the rupture risk of untreated aneurysms [15]. Lauric et al. attempted to explore a strategy to enhance radiomics performance and facilitate its adoption for aneurysm risk stratification [16]. An et al. investigated a novel semiautomatic prediction model for the rupture risk prediction of intracranial aneurysms with DSA [17]. However, to the best of our knowledge, there have been no reports of non-invasive MRA-based prediction of aneurysm rupture risk using radiomic analysis for follow-up MRA images prior to ruptures.

According to prospective cohort studies on the risk of intracranial aneurysm ruptures in Japan [18], 83% of patients with unruptured intracranial aneurysms were untreated, and an SAH occurred in merely 2% of patients during follow-up. Therefore, the dataset used in this study was imbalanced, which is similar to the percentages of the general Japanese population. The purpose of this preliminary study was to explore a radiomics prediction model for aneurysm rupture risk based on an imbalanced dataset of follow-up MRA images. An imbalanced adjustment training and test strategy was developed for this purpose.

2. Materials and Methods

The overall workflow of the proposed model for predicting the degree of intracranial aneurysm rupture is shown in Figure 1. Aneurysm contours of ruptured aneurysm (RA) and UA cases were delineated as regions of interest (ROI) on MRA images. We derived 486 image features from histogram and texture analyses (Section 2.2) within the ROI, selected three image features associated with UA and RA based on combinations of 11 features chosen using least absolute shrinkage and selection operator (LASSO) logistic regression [19] (Section 2.3), and input them into an SVM [19] to build prediction models for the degree of rupture. Finally, we evaluated rupture prediction models using a receiver operating characteristic (ROC) analysis based on a leave-one-out cross-validation test.

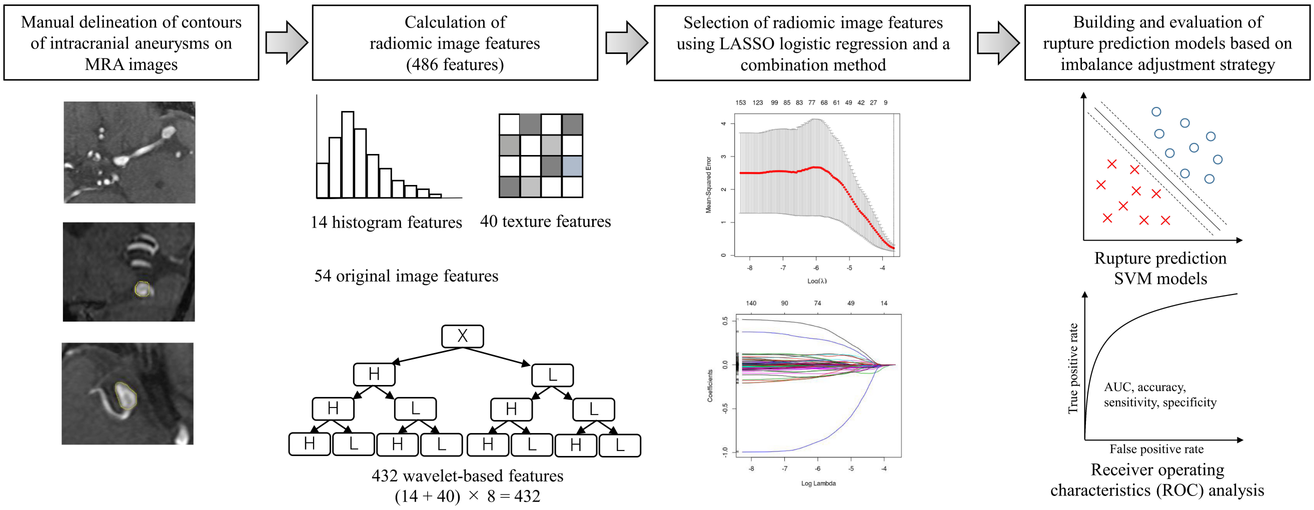

Figure 1. An overall workflow of a proposed model for prediction of degree of intracranial aneurysm rupture.

2.1. Patient Data

This retrospective study was performed with ethical approval from the Institutional Review Board of Kokura Memorial Hospital. We chose 113 follow-up MRA images prior to rupture, including 103 images of 18 UA cases and 10 images of RA cases, from 28 patients (35–92 years, median: 63 years) who underwent MRA for intracranial aneurysms examination. Patient characteristics are shown in Table 1. We selected mainly MCA aneurysms for the following two reasons based on a large Japanese cohort study (6697 aneurysms) [2]: (1) since the MCA is the most frequent location (36.2%) of intracranial aneurysms, it would not be difficult to collect them; (2) because MCA aneurysms relatively tend not to rupture, we can easily aggregate their follow-up images. The MRI images were acquired on a 3.0T scanner (SIGNA EXCITE HDxt 3.0T, GE Healthcare, Chicago, IL, USA). Parameters for the three-dimensional (3D) time-of-flight (TOF) MRA were set as follows: spoiled gradient–echo sequence with TR/TE/FA, 23 msec/3.4 msec/20°; FOV/Matrix, 200 × 229 mm/224 × 224; slice thickness/slice overlap, 1.2 mm/50%; ASSET factor, 2; actual bandwidth, 31 kHz. Anisotropic MRA images and ROI were transformed into isotropic images with an isovoxel size of $0.5 \times 0.5 \times 0.5$ mm^3, using cubic and shape-based interpolations [20], respectively. A neurosurgeon delineated the contours of the aneurysms as ROI for this study on the MRA images using the 3D slicer of open-source software [21]. The ROI of the aneurysms were employed to calculate radiomic image features on the MRA images. The aneurysm diameters ranged from 2 mm to 12 mm (median, 4.43 mm).

Table 1. Patient characteristics.

Characteristics	**Total of Patient Cohort**
No. of patients	28
No. of ruptured cases	10
No. of unruptured cases	18
Follow-up MRA images	
No. of images	113
No. of images for ruptured cases	10
No. of images for unruptured cases	103
Gender	
Male	9
Female	19
Age (year)	35–92 (median: 63)
Aneurysm diameter (mm)	2–12 (median: 4.43)

Table 1. *Cont.*

Characteristics	Total of Patient Cohort
Site of intracranial aneurysm	
Middle cerebral artery (MCA)	103
Internal carotid–posterior communicating artery (IC-PC)	5
Basilar artery (BA)	3
Anterior communicating artery (A-com)	2

2.2. Calculation of Radiomics Image Features

We calculated 486 image features, including 54 original image features and 432 wavelet-based features, within the ROI in the MRA images for the texture patterns. The original MRA images were requantized to 8 bits based on a look-up table between 0 and 255 and between minimum and maximum values within the aneurysm regions. As shown in Table S1, the 54 original radiomics features consisted of 14 histograms and 40 texture features. The 40 texture features were calculated from the gray-level co-occurrence matrix (GLCM), gray-level run-length matrix (GLRLM), gray-level size-zone matrix (GLSZM), and neighborhood gray-tone difference matrix (NGTDM). We derived 432 wavelet-based radiomics features from the same 54 features as the original features in each of the eight wavelet decomposition images. Wavelet decompositions were performed by applying either a low-pass filter (scaling function, L) or a high-pass filter (wavelet function, H) in the x, y, or z directions. The eight wavelet decomposition filters consisted of a combination of three filters using either a low-pass filter or high-pass filter in each direction.

2.3. Selection of Radiomic Features Using LASSO Logistic Regression

To avoid the risk of overfitting the prediction model, the significant radiomic features among the 486 image features were reduced to a number of image features using LASSO logistic regression [22]. LASSO logistic regression is an analytical method that reduces the estimator by setting the sum of the absolute values of the regression coefficients in the regularization term. As a result, LASSO logistic regression allows us to simultaneously perform both variable selection and regularization, improving the accuracy and interpretability of our predictions. The 486 radiomic features were narrowed down to 11 features using the LASSO logistic regression. This was because the maximum number of selected features, n, could be estimated using the number of training cases, N, using the following formula: $n < N/r$, where r is the events per variable [23], i.e., the number of training cases per feature in this study, as 5–10 [24]. In this study, because the number of training cases was 104 including UA and RA images (see Section 2.4), r, and the number of selected features were selected as 9 and 11, respectively. Finally, we selected three image features from the 11 features based on combinations of the top 1st–4th coefficients of the LASSO to avoid overfitting problems (Figure 3).

2.4. Building and Evaluating Rupture Prediction Models Based on Imbalance Adjustment Strategy

The number of UA and RA images employed in this study was imbalanced (103 and 10, respectively). Therefore, the synthetic minority oversampling technique (SMOTE) [25] was employed to balance the data between the RA and UA and prevent overfitting of the predictive model. Figure 2 shows an imbalance adjustment strategy with a leave-one-out cross-validation (LOOCV) test for rupture prediction models. The minority RA cases were oversampled by taking real RA cases and producing synthetic RA cases along the line segments accompanying any/all of the k minority RA's nearest neighbors. We randomly divided UA images into 50 and 53 images for the training and test sets, respectively. A case was selected as the test case from 10 patients with an RA. The remaining 9 RA cases were multiplied five times to 54 cases (45 synthetic cases + 9 original RA cases) for the training of the models. Ten sets, including 54 RA cases and 50 UA cases (total: 104 cases), were created for the training of 10 SVM models, which predict the degree of rupture in the same way. The 10 SVM models were applied to 10 test datasets with 1 RA case and 53 UA cases. The outputs of the 10 SVMs for the 10 RA cases were employed for the ROC analysis. On the other hand, the outputs of SVMs for each UA case were averaged, and the mean output of the SVMs was used for the ROC analysis when the same case was included in different test datasets.

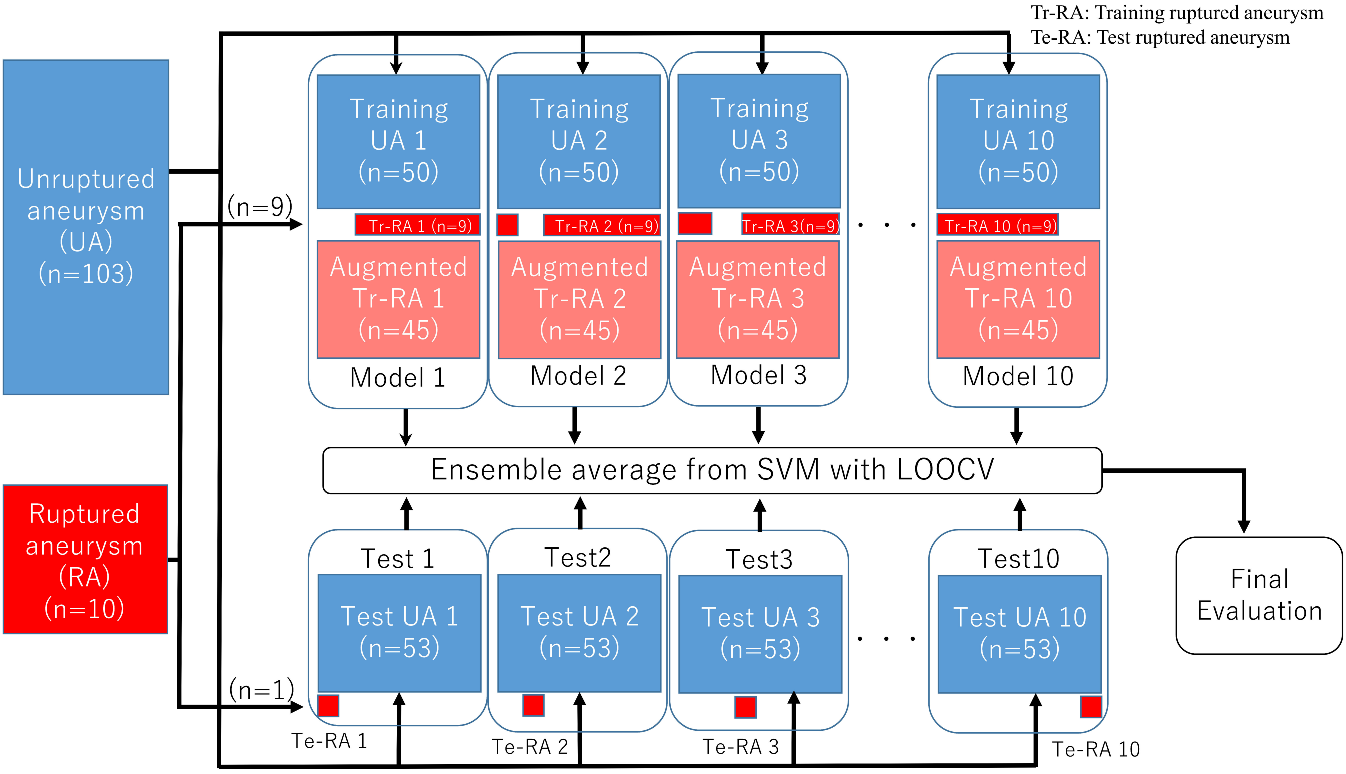

Figure 2. Building and evaluation of a rupture prediction model based on imbalance adjustment strategy.

The calculation times for the training and testing of the prediction model were around 8 h and 2 h, respectively, on a computer with a Core i7 2.93GHz central processing unit and 16 GB of memory. The prediction models were evaluated according to their AUCs, accuracy, sensitivity, and specificity. The AUC was obtained from the area under the ROC curve, which was a plot of sensitivity against (1—specificity), by changing the threshold values to SVM outputs. All calculations, except for the LASSO, were performed using the MATLAB-based Radiomics tools package (MATLAB 2019a, MathWorks, Natick, MA, USA). The R open-source software was used to calculate the LASSO.

3. Results

Table 2 shows the image features selected by the LASSO regression and their coefficients. All abbreviations are explained in Table S1. Eleven image features were selected using the LASSO regression from the 484 image features. Of these, two were texture features, and nine were histogram features. The image features with the highest LASSO regression coefficients were Energy.1 with a coefficient of 1.383, followed by LLH Variance.1 with a coefficient of 0.438 and LLH ZP with a coefficient of 0.239.

Table 2. Eleven radiomic features with their coefficients selected by LASSO. All abbreviations are explained in Table S1.

Radiomic Feature	Coefficient of LASSO
Energy.1 (texture/GLCM)	1.383
LLH Variance.1 (texture/GLCM)	0.438
LLH ZP (texture/GLSZM)	0.239
LLL MAD (histogram)	0.189
HLL ZP (texture/GLSZM)	0.107
LLH Variance (histogram)	0.0659
Uniformity (histogram)	0.0485
LLH Autocorrelation (texture/GLCM)	0.0311
LLH GLV (texture/GLRLM)	0.0260
HHH ZP (texture/GLSZM)	0.0153
LLH Contrast (texture/GLCM)	0.000211

"Energy.1" is the energy for a texture analysis, but "Energy" is that for a histogram. "Variance.1" is the variance for a texture analysis, but "Variance" is that for a histogram.

Figure 3 shows AUCs, accuracies, sensitivities, and specificities of 10 models with combinations of features selected by LASSO. The upper and lower bars show the results of the training and test models, respectively, for each combination of image features. The details are shown in Table S2. The combination of the top first, second, and third coefficients [Energy.1 (texture/GLCM) + LLH Variance.1 (texture/GLCM) + LLH ZP (texture/GLSZM)] reached a highest AUC of 0.971, an accuracy of 0.948, a sensitivity of 0.700, and a specificity of 0.953.

Figure 3. AUCs, accuracies, sensitivities, and specificities of 10 models with combinations of features selected by the top 1st–4th coefficients of LASSO.

Figure 4 depicts the scattered plots between the two features selected from the four image features for the RA and UA training cases. The image features for the RA and UA cases appear to have different distributions, where some of the RA or UA cases could be discriminated, but others overlapped.

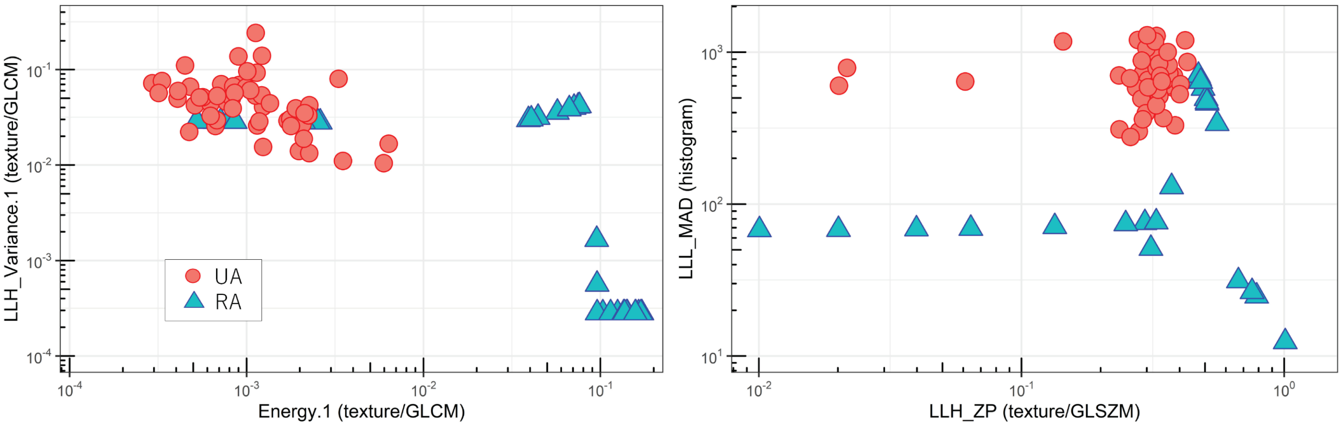

(a) (b)

Figure 4. Scattered plots of image features selected by LASSO for RA and UA training cases: (**a**) 1st and 2nd features; (**b**) 3rd and 4th features.

Figure 5 shows MRA images of the RA and UA cases. The intensities (mean: 240) around the aneurysm centers for this RA case are lower than that (mean: 456) of aneurysm surfaces shown in Figure 5a, whereas the UA case has higher intensities (mean: 655) around centers shown in Figure 5b.

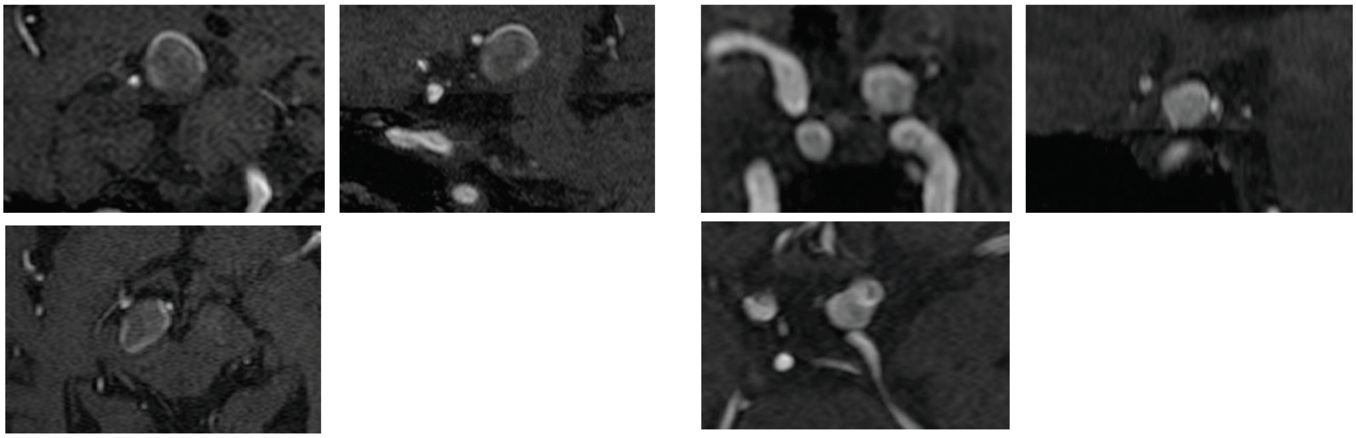

(a) (b)

Figure 5. MRA images of intracranial aneurysms: (**a**) an RA case; (**b**) a UA case.

4. Discussion

We investigated the radiomic features of MRA images associated with the rupture of intracranial aneurysms. Eleven radiomic image features associated with ruptured intracranial aneurysms were selected using LASSO, as shown in Table 2. The 11 features included eight texture features: Energy.1 (GLCM), LLH Variance.1 (GLCM), LLH ZP (GLSZM), HLL ZP (GLSZM), LLH Autocorrelation (GLCM), LLH GLV (GLRLM), HHH ZP (GLSZM), and LLH Contrast (GLCM) (GLCM:4, GLRLM:1, GLSZM:3); and three histogram features: LLL MAD, LLH variance, and uniformity. These basically assessed the voxel-value heterogeneity in the ROI, such as aneurysms, but from different theories. Finally, we chose a combination of three features, Energy.1 (texture/GLCM), LLH Variance.1 (texture/GLCM), and LLH ZP (texture/GLSZM), to achieve the highest AUC of 0.971, accuracy of 0.948, sensitivity of 0.700, and specificity of 0.953.

Energy.1 (GLCM) is a measure of squared-voxel-value-wise intensity patterns in an ROI based on the GLCM, which represents the number (or frequency) of co-occurrences for combinations of two gray levels occurring in neighboring voxels in a specific direction. Variance.1 (GLCM) is a measure of squared-voxel-value-wise variation patterns in the ROI based on the GLCM. The zone percentage (ZP) (GLSZM) is a measure of area-wise variation patterns based on GLSZM, which represents the same voxel-value areas, that is, the number of connected voxels with the same voxel values. The ZP measures the fraction of the number of realized zones and the maximum number of potential zones [26]. Therefore, because voxel values within an ROI have a more spatially coarse heterogeneity, the ZP features could be larger. MAD (histogram) is a measure of the deviation values of all intensity values minus the mean value obtained from the histogram of an ROI. The Variance (histogram) used is that obtained from the histogram of an ROI.

Because RA cases may have turbulent flow around the aneurysm centers [27,28], the intensities around the centers could be lower than that of aneurysm surfaces in MRA images [29,30] as shown in Figure 5a. This phenomenon could result in a relatively higher Energy.1 (GLCM) and LLH ZP LLH; however, some UA cases overlapped with the RA cases, as shown in Figure 4. Variance.1 (GLCM) and LLL MAD (histogram) showed higher values for some UA cases, as shown in Figure 4, because the UA cases may have higher intensities around centers in MRA images as shown in Figure 5b.

There are several reports on the prediction of aneurysm ruptures using radiomics of CTA and DSA, mainly concerning morphological features [9–17]; however, to the best of our knowledge, no study has been conducted on MRA, and, therefore, our study appears to be the first. Their AUCs ranged from 0.738 to 0.860 in the validation tests, whereas that in our study was 0.977.

This study had four limitations. First, we included a small number of UA and RA cases, especially the number of RA cases. Thus, the specificity was high (0.983), but the sensitivity was low (0.700). Therefore, the number of cases should be increased, collecting cases from different institutions to avoid false-negative cases so that the UA and RA cases can have almost the same, and enough, numbers. When collecting them, we should consider various locations (for example, anterior cerebral arteries, posterior cerebral arteries, and posterior communicating artery) and various sizes from <5 mm to >20 mm, which show different hazard ratios to rupture risks [18]. In addition, we should compare the results with and without using the SMOTE to investigate its impact on the final result. Second, a feature selection and machine learning methods were employed in this study. Many feature selections and machine learning approaches should be attempted to increase the number of options for installing the proposed approach in different institutions, depending on their clinical policy [19]. Third, we focused on the intensity heterogeneity in intracranial aneurysms using histogram and texture features but did not employ morphological features because manual contours of aneurysms may cause intra- and inter-observer variabilities [8], which reduces feature reliability. The development or use of automated segmentation approaches [31] is necessary for the use of the morphological features, which may increase the performance of the proposed approach. Fourth, a neurosurgeon delineated aneurysm contours on the MRA images. Therefore, the contours should be verified by different neurosurgeons or neuroradiologists in the next study.

5. Conclusions

We performed the first preliminary study to develop prediction models for aneurysm rupture risks using radiomics analysis based on follow-up MRA images. We found significant radiomic features which were associated with the prediction of aneurysm rupture. The AUC, accuracy, sensitivity, and specificity of the prediction model were 0.971, 0.948, 0.700, and 0.953, respectively. By overcoming the limitations mentioned above, we can develop a more robust radiomics analysis system with higher AUC, accuracy, sensitivity, and specificity. This radiomics analysis system could be utilized to predict aneurysm rupture risks for SAH prevention during follow-up MRA examinations.

Supplementary Materials: The following supporting information can be downloaded at: https://www.mdpi.com/article/10.3390/app12178615/s1. Table S1. Radiomic features used in the calculation. Table S2. AUCs, sensitivity, specificity, and accuracy of a proposed rupture prediction model from training and test images with top combinations of LASSO ranking.

Author Contributions: Conceptualization: M.Y. and H.A.; methodology: M.Y. and H.A.; software: M.Y., T.K., and A.U.; formal analysis: M.Y. and H.A.; writing—original draft preparation: M.Y. and H.A.; writing—review and editing: M.Y., H.A., and T.K. All authors have read and agreed to the published version of the manuscript.

Funding: This study was supported by a JSPS KAKENHI grant (Number JP20K08084).

Institutional Review Board Statement: This retrospective study was performed with an ethical approval from the Institutional Review Board (IRB) of Kokura Memorial Hospital. According to the IRB, informed consents were waived due to the retrospective nature, and all patients' data were used anonymously. All procedures in the studies involving human participants were performed in accordance with the ethical standards of the institutional and/or national research committee and the 1964 Helsinki Declaration and its later amendments or comparable ethical standards. This article does not involve any animal study performed by the authors.

Informed Consent Statement: According to the IRB, informed consents were waived due to the retrospective nature.

Data Availability Statement: The data that support the findings of this study are available from the corresponding author upon reasonable request.

Acknowledgments: The authors are grateful to Hideo Chihara, who is a neurosurgeon in Kokura Memorial Hospital (current affiliation: Hikone Municipal Hospital) for selecting ruptured and unruptured aneurysm cases and determining aneurysm regions. The authors would like to say many thanks to all the members of the Arimura Laboratory (http://web.shs.kyushu-u.ac.jp/~arimura/ (accessed on 27 August 2022)), whose comments contributed to this study.

Conflicts of Interest: The authors declare no conflict of interest.

References

1. van Gijn, J.; Rinkel, G.J. Subarachnoid haemorrhage: Diagnosis, causes and management. *Brain* **2001**, *124*, 249–278. [CrossRef] [PubMed]
2. UCAS Japan Investigators; Morita, A.; Kirino, T.; Hashi, K.; Aoki, N.; Fukuhara, S.; Hashimoto, N.; Nakayama, T.; Sakai, M.; Teramoto, A.; et al. The natural course of unruptured cerebral aneurysms in a Japanese cohort. *N. Engl. J. Med.* **2012**, *366*, 2474–2482. [CrossRef] [PubMed]
3. The Japan Stroke Society. *Japanese Guidelines for the Management of Stroke 2015*; The Japan Stroke Society: Kyowa Kikaku, Tokyo, 2015.
4. Raaymakers, T.W.; Rinkel, G.J.; Limburg, M.; Algra, A. Mortality and morbidity of surgery for unruptured intracranial aneurysms: A meta-analysis. *Stroke* **1998**, *29*, 1531–1538. [CrossRef] [PubMed]
5. Nakagawa, D.; Nagahama, Y.; Policeni, B.A.; Raghavan, M.L.; Dillard, S.I.; Schumacher, A.L.; Sarathy, S.; Dlouhy, B.J.; Wilson, S.; Allan, L.; et al. Accuracy of detecting enlargement of aneurysms using different MRI modalities and measurement protocols. *J. Neurosurg.* **2018**, *130*, 559–565. [CrossRef] [PubMed]
6. Sailer, A.M.; Wagemans, B.A.; Nelemans, P.J.; de Graaf, R.; van Zwam, W.H. Diagnosing intracranial aneurysms with MR angiography: Systematic review and meta-analysis. *Stroke* **2014**, *45*, 119–126. [CrossRef]
7. Keedy, A. An overview of intracranial aneurysms. *McGill J. Med.* **2006**, *9*, 141–146. [CrossRef]
8. Groth, M.; Forkert, N.D.; Buhk, J.H.; Schoenfeld, M.; Goebell, E.; Fiehler, J. Comparison of 3D computer-aided with manual cerebral aneurysm measurements in different imaging modalities. *Neuroradiology* **2013**, *55*, 171–178. [CrossRef]
9. Liu, Q.L.; Jiang, P.; Jiang, Y.H.; Ge, H.J.; Li, S.L.; Jin, H.W.; Li, Y.X. Prediction of Aneurysm Stability Using a Machine Learning Model Based on PyRadiomics- Derived Morphological Features. *Stroke* **2019**, *50*, 2314–2321. [CrossRef]
10. Ludwig, C.G.; Lauric, A.; Malek, J.A.; Mulligan, R.; Malek, A.M. Performance of Radiomics derived morphological features for prediction of aneurysm rupture status. *J. Neurointerv. Surg.* **2021**, *13*, 755–761. [CrossRef]
11. Alwalid, O.; Long, X.; Xie, M.; Yang, J.; Cen, C.; Liu, H.; Han, P. CT Angiography-Based Radiomics for Classification of Intracranial Aneurysm Rupture. *Front. Neurol.* **2021**, *12*, 619864. [CrossRef]
12. Zhu, D.; Chen, Y.; Zheng, K.; Chen, C.; Li, Q.; Zhou, J.; Jia, X.; Xia, N.; Wang, H.; Lin, B.; et al. Classifying Ruptured Middle Cerebral Artery Aneurysms With a Machine Learning Based, Radiomics-Morphological Model: A Multicentral Study. *Front. Neurosci.* **2021**, *15*, 721268. [CrossRef] [PubMed]

13. Tong, X.; Feng, X.; Peng, F.; Niu, H.; Zhang, B.; Yuan, F.; Jin, W.; Wu, Z.; Zhao, Y.; Liu, A.; et al. Morphology-based radiomics signature: A novel determinant to identify multiple intracranial aneurysms rupture. *Aging (Albany N. Y.)* **2021**, *13*, 13195–13210. [CrossRef] [PubMed]
14. Ou, C.; Chong, W.; Duan, C.Z.; Zhang, X.; Morgan, M.; Qian, Y. A preliminary investigation of radiomics differences between ruptured and unruptured intracranial aneurysms. *Eur. Radiol.* **2021**, *31*, 2716–2725. [CrossRef] [PubMed]
15. Ou, C.; Li, C.; Qian, Y.; Duan, C.Z.; Si, W.; Zhang, X.; Li, X.; Morgan, M.; Dou, Q.; Heng, P.A. Morphology-aware multi-source fusion-based intracranial aneurysms rupture prediction. *Eur. Radiol.* **2022**, *32*, 5633–5641. [CrossRef]
16. Lauric, A.; Ludwig, C.G.; Malek, A.M. Enhanced Radiomics for Prediction of Rupture Status in Cerebral Aneurysms. *World Neurosurg.* **2022**, *159*, e8–e22. [CrossRef]
17. An, X.; He, J.; Di, Y.; Wang, M.; Luo, B.; Huang, Y.; Ming, D. Intracranial Aneurysm Rupture Risk Estimation With Multidimensional Feature Fusion. *Front. Neurosci.* **2022**, *16*, 813056. [CrossRef]
18. Etminan, N.; Rinkel, G.J. Unruptured intracranial aneurysms: Development, rupture and preventive management. *Nat. Rev. Neurol.* **2016**, *12*, 699–713. [CrossRef]
19. Hastie, T.; Tibshirani, R.; Friedman, J. *The Elements of Statistical Learning-Data Mining, Inference, and Prediction*, 2nd ed.; Springer: New York, NY, USA, 2008.
20. Herman, G.T.; Zheng, J.; Bucholtz, C.A. Shape-based interpolation. *IEEE Comput. Graph. Appl.* **1992**, *12*, 69–79. [CrossRef]
21. 3D Slicer. Available online: https://slicer.readthedocs.io/en/latest/index.html (accessed on 27 August 2022).
22. Tibshirani, R. Regression Shrinkage and Selection via the Lasso. *J. R. Statist. Soc. B* **1996**, *58*, 267–288. [CrossRef]
23. Peduzzi, P.; Concato, J.; Kemper, E.; Holford, T.R.; Feinstein, A.R. A simulation study of the number of events per variable in logistic regression analysis. *J. Clin. Epidemiol.* **1996**, *49*, 1373–1379. [CrossRef]
24. Arimura, H.; Soufi, M.; Ninomiya, K.; Kamezawa, H.; Yamada, M. Potentials of radiomics for cancer diagnosis and treatment in comparison with computer-aided diagnosis. *Radiol. Phys. Technol.* **2018**, *11*, 365–374. [CrossRef] [PubMed]
25. Chawla, N.V.; Bowyer, K.W.; Hall, L.O.; Kegelmeyer, W.P. SMOTE: Synthetic Minority Over-sampling Technique. *J. Artif. Intell. Res.* **2002**, *16*, 321–357. [CrossRef]
26. Zwanenburg, A.; Vallières, M.; Abdalah, M.A.; Aerts, H.J.W.L.; Andrearczyk, V.; Apte, A.; Ashrafinia, S.; Bakas, S.; Beukinga, R.J.; Boellaard, R.; et al. The Image Biomarker Standardization Initiative: Standardized Quantitative Radiomics for High-Throughput Image-based Phenotyping. *Radiology* **2020**, *295*, 328–338. [CrossRef]
27. Soldozy, S.; Norat, P.; Elsarrag, M.; Chatrath, A.; Costello, J.S.; Sokolowski, J.D.; Tvrdik, P.; Kalani, M.Y.S.; Park, M.S. The biophysical role of hemodynamics in the pathogenesis of cerebral aneurysm formation and rupture. *Neurosurg. Focus* **2019**, *47*, E11. [CrossRef]
28. Zhang, H.; Liang, S.; Lv, X. Intra-aneurysmal thrombosis and turbulent flow on MRI of large and giant internal carotid artery aneurysms. *Neurosci. Inform.* **2021**, *1*, 100027. [CrossRef]
29. Arimura, H.; Li, Q.; Korogi, Y.; Hirai, T.; Abe, H.; Yamashita, Y.; Katsuragawa, S.; Ikeda, R.; Doi, K. Automated computerized scheme for detection of unruptured intracranial aneurysms in three-dimensional magnetic resonance angiography. *Acad. Radiol.* **2004**, *11*, 1093–1104. [CrossRef] [PubMed]
30. Baghaie, A.; Schnell, S.; Bakhshinejad, A.; Fathi, M.F.; D'Souza, R.M.; Rayz, V.L. Curvelet Transform-based volume fusion for correcting signal loss artifacts in Time-of-Flight Magnetic Resonance Angiography data. *Comput. Biol. Med.* **2018**, *99*, 142–153. [CrossRef] [PubMed]
31. Yuan, W.; Peng, Y.; Guo, Y.; Ren, Y.; Xue, Q. DCAU-Net: Dense convolutional attention U-Net for segmentation of intracranial aneurysm images. *Vis. Comput. Ind. Biomed. Art.* **2022**, *5*, 9, Erratum in *Vis. Comput. Ind. Biomed. Art.* **2022**, *5*, 12. [CrossRef]